Polymeric C_3N_4 and O-modified C_3N_4 for Selective Photocatalytic Oxidation of Alcohols to Aldehydes: Photoelectrochemical and EPR Features

G. Marcì[1*], E.I. García-López[1], F.R. Pomilla[1], L. Palmisano[1], A. Zaffora[2], M. Santamaria[2], I. Krivtsov[3,4], M. Ilkaeva[5], Z. Barbieriková[6],V. Brezová[6]

[1] *"Schiavello-Grillone" Photocatalysis Group. Dipartimento di Energia, Ingegneria dell'informazione e modelli Matematici (DEIM), Università di Palermo, Viale delle Scienze, 90128 Palermo, Italy.*

[2] *Electrochemical Materials Science Laboratory, Dipartimento di Ingegneria Civile, Ambientale, Aerospaziale e dei Materiali (DICAM), Università di Palermo, Viale delle Scienze, 90128 Palermo, Italy.*

[3] *Department of Chemical and Environmental Engineering, University of Oviedo, 33006 Oviedo, Spain.*

[4] *Nanotechnology Education and Research Center, South Ural State University, 454080 Chelyabinsk, Russia.*

[5] *Department of Organic and Inorganic Chemistry, University of Oviedo, 33006 Oviedo, Spain.*

[6] *Faculty of Chemical and Food Technology, Slovak University of Technology in Bratislava, Radlinského 9, SK-81237 Slovak Republic.*

*Corresponding author: giuseppe.marci@unipa.it

Abstract

Four different C_3N_4 specimens have been prepared, a bulk one (MCN), a thermally etched (MCN-TE), a solid prepared by hydrothermally treating MCN with H_2O_2 (MCN-H_2O_2) and a polymeric carbon nitride-hydrogen peroxide adduct (MCN-TE-H_2O_2). Photoelectrochemical studies revealed that MCN-TE represented the best material in terms of band gap energy and photoconductivity,

whereas MCN-H$_2$O$_2$ was defective and evidenced a poor mobility of carriers. EPR studies showed a maximum generation of reactive oxygen species irradiating the MCN-TE sample. The photocatalytic activity of these materials in the selective oxidation of three different alcohols to the corresponding aldehydes, both under UV and natural solar light, showed that the highest conversion was obtained in the presence of the MCN-TE sample, whereas the most selective was MCN-TE-H$_2$O$_2$. Under solar light irradiation the performances of the powders were generally better than those carried under UV light. The characterization of the C$_3$N$_4$-based materials well justified their photocatalytic activity, where the pristine C$_3$N$_4$ materials were more active but less selective than those prepared in the presence of H$_2$O$_2$.

1. Introduction

The application of photocatalysis to water and air remediation by using TiO$_2$ has been widely studied due to unselectivity of titania which gives rise to the complete mineralization of pollutants. However, photocatalysis can also be used to selectively oxidize and/or reduce a substrate producing higher value chemicals [1,2]. TiO$_2$ under UV irradiation readily forms hydroxyl radicals, the main reactive oxygen species (ROS) in photocatalysis, which unselectively attack organic species. An alternative photocatalyst with lower oxidant ability could avoid the complete oxidation of the substrate. Moreover, in synthetic photocatalysis the use of solar light as the radiation source could maximize the green approach to the process.

In this context, a new photocatalytic material with appropriate thermodynamic requirements to perform selective partial oxidations is polymeric carbon nitride (C$_3$N$_4$). Antonietti et al. proposed the use of this metal-free semiconductor as heterogeneous photocatalyst [3]. This layered material consisting of conjugated two-dimensional tri-*s*-triazine-based C-N groups forming graphite-like structures is chemically and thermally robust and easily prepared by thermal polymerization of cheap and abundant C,N-rich precursors. C$_3$N$_4$ shows a lower band gap than TiO$_2$ (ca. 2.7 eV), hence

sunlight can be used to initiate photocatalytic reactions [4]. The favorable energies of its conduction (CB) and valence (VB) bands and the absence of hydroxyl groups on the surface, which would favour the direct formation of the unselective $^\bullet$OH radicals, make C_3N_4 an optimal candidate to be utilized in selective photocatalytic oxidations even in aqueous solutions [5,6]. The electrons promoted into the CB of C_3N_4 are able to reduce O_2 to form the superoxide radical anion ($O_2^{\bullet-}$) and successively H_2O_2. On the contrary, the potential of the holes generated on the VB is not sufficient to oxidize OH^- to form $^\bullet$OH radicals. However, the performance of C_3N_4 is still hindered by its low electrical conductivity, lack of absorption above 460 nm and recombination of photogenerated excitons [7-9]. EPR represents an appropriate tool to determine the course of paramagnetic charge carriers and to investigate the photogenerated charge carrier behaviour, especially the events of photoinduced electrons and holes at the material-reactant interface [9-12]. In order to improve the C_3N_4 performance as photocatalyst several approaches have been explored to improve/modify/optimize its structure. Incorporation of specific substituents and functional groups [13] could not only increase the specific surface area (SSA), but also modify the band gap energy and/or improve the electron-hole separation. Several morphologies of C_3N_4 have been obtained by different synthetic routes [14]. Non-metallic elements incorporated into the C_3N_4 layer, induce superior performances [15-19]. The O-doping process has been reported as an effective method to enlarge surface area and improve the conductivity for the enhancement of catalytic performance [20-24]. The C_3N_4 absorption band edges were red-shifted with increasing oxygen dopants. Also, a post-treatment of the bulk C_3N_4 can produce oxygen-doped C_3N_4 with a narrower band gap and a higher specific surface area, exhibiting photoactivities improved by four times compared to the pristine C_3N_4 for dye degradation or hydrogen evolution under visible-light irradiation [21].

In the present work, four different C_3N_4 photocatalysts were studied. A polymeric C_3N_4 obtained by melamine annealing (MCN), a thermally etched material, resulted from a further calcination of MCN in air (MCN-TE), a stable adduct composed of the thermally etched material with H_2O_2 (MCN-

80 TE-H_2O_2) and a C_3N_4 prepared in the presence of H_2O_2 under hydrothermal conditions (MCN-H_2O_2).

81 The aim of the work was to understand the physico-chemical differences between these four

82 specimens in terms of band gap energy and capability to generate reactive oxygen species (ROS)

83 responsible for the photocatalytic activities. Physico-chemical characterization studies help to justify

84 the photocatalytic activities in water of the four powders for the partial oxidation of three organic

85 alcohols to their corresponding aldehydes.

86

87 **2. Experimental**

88 *2.1. Preparation of the photocatalysts*

89 The polymeric carbon nitride labelled as MCN, was prepared via thermal condensation of

90 melamine as reported before [4]. Melamine (10g) was placed in a covered ceramic crucible and heated

91 at 520°C for 2 hours. MCN was then subjected to thermal etching in an uncovered ceramic bowl

92 heated at 3 °C min^{-1} and maintained for 4 h at 500° C. The obtained light yellow powder was

93 designated as MCN-TE [4]. An oxidized C_3N_4, labelled MCN-H_2O_2, was prepared according to the

94 procedure described before [23], where 1 g of MCN was dispersed in 80 mL of 30% H_2O_2 solution.

95 The suspension was placed in a 100 mL Teflon vessel in an autoclave and hydrothermally treated

96 (130 °C for 24 h). The powder was washed several times with hot water to remove the H_2O_2 in excess

97 and finally dried at 60 °C. An alternative material was prepared as before descrived [25-27], by

98 dispersing 2.8 g of MCN-TE in 50 mL of H_2O_2 aqueous solution (30 wt%) in an open beaker while

99 heating at 70 °C until complete evaporation of the liquid. The obtained solid was washed with water

100 until absence of H_2O_2 in the washing liquid, filtered and finally dried at 80 °C for 24 h giving the

101 MCN-TE-H_2O_2 powder.

102 *2.2. Characterisation of the photocatalysts*

103 Powder XRD patterns were registered in an X'pert PANanalytical diffractometer, using a Ni

104 filtered Cu-Kα radiation source and PixCel1D (tm) detector.

105 Infrared spectra of the samples were recorded with 4 cm^{-1} resolution using an ATR module in a Varian

106 620-IR spectrometer. X-ray photoelectron spectroscopy (XPS) was measured by a SPECS system

107 equipped with a Hemispherical Phoibos analyser operating in a constant pass energy, using MgKα

108 radiation (h·ν = 1253.6 eV). The absence of C–C bonds in carbon nitride made possible taking a

109 signal of adventitious carbon at 284.8 eV as a reference. The elemental composition was estimated

110 from the deconvoluted high-resolution XPS data, eliminating the contribution of the adventitious

111 carbon signal. The solid-state ^{1}H MAS NMR, ^{13}C, ^{1}H–^{13}C CPMAS and ^{1}H–^{15}N CPMAS NMR spectra

112 were registered using a Bruker Avance III 400WB spectrometer. The temperature programmed

113 desorption mass-spectroscopic (TPD-MS) analysis was carried out with help of a Micromeritics

114 Autochem II 2920 system coupled with a ThermoStar mass spectrometer. For the analysis, 50 mg of

115 powdered samples was heated from 35 °C to 500 °C at 5 °C min^{-1} in helium flowing through the

116 sample at a rate of 10 mL min^{-1}. A Shimadzu UV-2401 PC spectrophotometer equipped with an

117 integrated sphere was used to obtain diffuse reflectance spectra (DRS) by using $BaSO_4$ as reference.

118 A Micromeritics ASAP 2020 was used to obtain adsorption-desorption isotherms of N_2 at 77 K.

119 Specific surface area (SSA) was calculated from the nitrogen adsorption data by BET equation.

120 Photoelectrochemical characterization was carried out by using a 450 W UV-VIS Xenon lamp

121 coupled with a Kratos monochromator, which allows a monochromatic irradiation of the specimen

122 that is filtered through a quartz window present in the cell. A two phase lock-in amplifier was used,

123 coupled with a mechanical chopper (frequency of 13 Hz), allowing to extract photocurrent signals

124 from the total current circulating in the cell. To estimate the optical band gap, photocurrent spectra

125 were corrected for the relative photon flux of the light source at each wavelength. All the

126 photoelectrochemical measurements were carried out in 0.1 M ammonium biborate tetrahydrate

127 electrolyte (ABE, $(NH_4)_2B_4O_7 \cdot 4H_2O$; pH ~ 9) at room temperature (RT) with a three-electrode

128 configuration using a Pt wire as counter electrode and Ag/AgCl/sat. KCl electrode (0 V vs Ag/AgCl

129 = 0.197 V *vs* SHE) as the reference electrode. For these measurements, the different C_3N_4

130 photocatalysts were deposited on carbon paper (Toray 40% wet Proofed-E-Tek). The EPR spectra of

C3N4 powders at RT or at 100K in dark or upon continuous *in situ* UV photoexcitation (λ_{max}=365 nm; Bluepoint LED, Hönle UV Technology) were measured by EMX EPR spectrometer (Bruker) operating in X-band at 100 kHz field modulation in the standard TE$_{102}$ (ER 4102 ST) rectangular cavity using thin-walled quartz EPR tubes (Bruker). The temperature was lowered to 100 K by the temperature unit ER 4111 VT (Bruker), with liquid nitrogen as the refrigerant. The EPR spin trapping technique, using 5,5-dimethyl-1-pyrroline *N*-oxide (DMPO) spin trap, was applied to detect non-persistent radical intermediates generated upon UV (λ_{max}=365 nm) or visible exposure of the catalysts suspended in water or dimethyl sulfoxide (DMSO)/water mixed solvent (80:20 v:v) at 295 K. The photoexcitation of aerated suspensions containing both photocatalyst and DMPO took place in the resonator of the EPR spectrometer (EMXPlus, Bruker) and the generation of the spin-adducts was monitored *in situ*. The concentration of spin-adducts was evaluated from the double-integrated spectra using the calibration curve obtained from the EPR spectra of 4-hydroxy-2,2,6,6-tetramethylpiperidine *N*-oxyl solutions measured under strictly identical experimental conditions. Multi-component EPR spectra were analyzed and simulated using Winsim2002 software [28]. The detailed information on EPR measurements is described in [29].

2.3. Photocatalytic reactivity

Photocatalytic experiments were carried out in a water-cooled Pyrex reactor containing 150 mL of aqueous suspension irradiated with six Actinic BL TL MINI 15 W/10 Philips fluorescent lamps (λ_{max}=365 nm) at RT under air, in the system previously reported [4,26]. The partial oxidation of three organic alcohols , *i.e.* 4-methoxy benzyl alcohol (4-MBA), cinnamyl alcohol (CA) and 5-hydroxymethylfurfural (HMF), to their corresponding aldehydes *i.e.* 2,5-furandicarboxaldehyde (FDC), 4-methoxy benzylaldehyde (4-MBAL) and cinnamaldehyde (CAL), respectively, was studied at 0.5 mM initial alcohol concentration at natural pH. The amount of photocatalyst used was 50 mg, enough to absorb all the entering photons in the photoreactor. The impinging radiation energy in the range 315-400 nm was measured by a radiometer Delta Ohm DO9721 (average value ca. 8 W m^{-2}). Natural sunlight was also used as the radiation source in an alternative 125 mL Pyrex batch

photoreactor containing 75 mL of 0.5 mM alcohol suspension in the presence of the photocatalyst. The suspensions were continuously stirred and aliquots of approximately 2.5 mL were withdrawn for analyses every 30 min. The photon flux in the range of 315-400 nm, which largely determines the reactivity of C_3N_4, was measured every 10 min throughout the runs, and the cumulative energy (E) was estimated based on the obtained data. The E value allows the comparison of photoreactivity results obtained under natural sunlight irradiation at different meteorological conditions. It is given by:

$$E = \int_0^t I(t)\, dt \tag{1}$$

where "$I(t)$" is the instantaneous photon flow and "t" the irradiation time. The values of "$I(t)$" were calculated from the recorded values of irradiance, $UVG(t)$, by using the following relationship:

$$I(t) = UVG(t) \times S \tag{2}$$

where "S" is the total irradiated surface and "UVG" is the irradiance (315-400 nm wavelength range) [30]. The aliquots of reacting suspensions were filtered and analysed by HPLC. HMF and derived molecules were analysed by a Thermo Scientific Dionex UltiMate 3000 HPLC equipped with a Diode Array detector and a REZEK ROA organic acid column with a 2.5 mM H_2SO_4 aqueous solution mobile phase (flow rate 0.6 mL min^{-1}). The aromatic species were analyzed by a Beckman coulter HPLC with a Diode Array detector. The column was a Phenomenex KINETEK 5 μm C18 and the eluent (0.8 mL min^{-1}) a mixture of acetonitrile and 13 mM trifluoroacetic acid (20:80 v:v). Standards purchased from Sigma-Aldrich with a purity > 99% were used to identify the products and to obtain the calibration curves.

3. Results and Discussion

All the samples showed the typical XRD patterns of C_3N_4, suffering negligible changes after the thermal etching or H_2O_2 treatment (see Fig. S1 in Supplementary Material), which is also corroborated by FTIR spectroscopy (Fig. S2). The SSA of the powders were 7, 94, 28 and 70 $m^2 \cdot g^{-1}$ for MCN, MCN-TE, MCN-H_2O_2 and MCN-TE-H_2O_2, respectively (Fig. S3). A dramatic difference was observed between ^1H MAS NMR spectra for MCN and the other samples attributed to the weakening of the hydrogen bonding between the $C_3N_4H_x$ species as evidenced by the decrease of intensity of the peak at 9.2 ppm [26] (Fig. S4). The assignation of chemical shifts of C and N atoms constituting carbon nitride is shown in Fig. S5. ^{13}C MAS NMR spectra (Fig. S6) and the ^{13}C-^1H MAS NMR (Fig. S7) show that the incorporation of oxygen heteroatom inside the C_3N_4 skeleton is unlike. Neither the ^{15}N-^1H CPMAS NMR indicated the presence of new nitrogen-containing groups after the treatment of MCN (Fig. S8). The XPS data, although not manifesting significant changes of the oxidation state of C, clearly demonstrate the redistribution of N-species and increased O content in the MCN-H_2O_2 sample with respect to the pristine one (Fig. S9, Table S1). Moreover, the surface elemental composition analysis of this material reveals a high C/N ratio indicating the presence of N-vacancies (Table S1). Noteworthy, TPD data show that, apart from the shift of the water desorption maximum to higher temperatures for the MCN-H_2O_2 sample, its decomposition starts at lower temperature, which is evident by the evolution of 17 amu (NH_3^+). Also, the appearance of 42 amu and 43 amu in the mass-spectra might be assigned to the CNO^+ and $CNOH^+$ species (Fig. S10). Hence, it is suggested that the treatment of MCN with H_2O_2 under hydrothermal conditions provokes oxidation of the surface carbon nitride functionalities leading to the reduced N content and, possibly to the formation of surface C-N-O bonds, which could be the reason of the redistribution of N-species evidenced from the XPS analysis.

X-band EPR spectra of the C_3N_4-based powders measured at 100 K before UVA irradiation indicated an effect of H_2O_2 treatment on the character of paramagnetic defects generated during the synthetic procedures (Fig. S11). A single Lorenztian line with $g = 2.0033$ assigned to the unpaired

208 electrons in the aromatic rings of carbon atoms (CB electrons) in the localized π-states of typical

209 heptazine g-C_3N_4 dominates the EPR spectra of non-exposed MCN and MCN-TE samples [31]. The

210 EPR spectra for the MCN and MCN-TE photocatalysts are analogous, only the intensities were higher

211 in the case of the thermally etched material possibly due to the increased concentration of defects. On

212 the contrary, both MCN-TE-H_2O_2 and MCN-H_2O_2 exhibited similar and more complex EPR spectra

213 (Fig.S11), fully compatible with those measured previously for the analogously prepared oxygen

214 functionalized C_3N_4 [23]. The EPR signals observed for the MCN-TE-H_2O_2 and MCN-H_2O_2 powders

215 (stable at RT with even better resolution compared to 100 K) may be assigned to the paramagnetic

216 species formed by the oxidation of carbon/nitrogen sites in the C_3N_4 network with H_2O_2. UVA

217 exposure of all C_3N_4-based samples at 100 K resulted in the increased intensity of the single line at g

218 $= 2.0033$ indicating the photoinduced generation of the CB electrons or radicals in the polymer

219 network. The additional signals found in the EPR spectra of MCN-TE-H_2O_2 and MCN-H_2O_2

220 remained rather intact upon exposure (Fig.S11).

221 The optical properties of the samples have been investigated by UV-Vis diffuse reflectance spectra

222 (DRS). The energy band-gap values were obtained by extrapolating a linear fitting in the Tauc plot.

223 The values obtained were ca. 2.7 eV for MCN, 2.8 eV for MCN-TE, whereas slightly increased to ca.

224 2.9 eV and 3.0 for MCN-H_2O_2 and MCN-TE-H_2O_2, respectively. Noteworthy, the two last materials

225 showed in the Tauc plot some electronic transitions in the visible part of the spectrum, attributed to

226 some electronic states located between the VB and the CB (Fig. S12).

227 Generation and transport of photoexcited charge carriers in the photocatalytic process can be

228 indirectly monitored by photoelectrochemical measurements. In fact, the photocurrent yield "Q_{ph}"

229 can be calculated according to [32] and for photon energy close to the absorption edge, the

230 dependence of the light absorption coefficient on hν is described by the following relationship [33]:

231

232 $(Q_{ph} h\nu)^n \propto (h\nu - E_g^{opt})$ (3)

233

234 in which E_g^{opt} is the optical band gap and the exponent n assumes different values depending on the

235 involved optical transitions. Therefore, the photocurrent yield depends on wavelength and on the

236 transport properties of the material. Fig. 1(A) shows current transients under monochromatic

237 irradiation, recorded at 0.5 V vs Ag/AgCl for all the tested samples. The highest photocurrent was

238 recorded for MCN-TE, while MCN-H_2O_2 had the worst performance with a strong recombination

239 under low wavelength suggesting a low photocarriers separation efficiency. Notably, for $\lambda = 420$ nm,

240 corresponding to a photon energy of 2.95 eV and therefore higher than the band gap estimated by

241 DRS (see Fig. S12) a very low photocurrent (few nA) was recorded for MCN-H_2O_2, while no

242 photocurrent was recorded for MCN-TE-H_2O_2. This experimental finding suggests a strong

243 localization of allowed energy levels close to valence and conduction band edges of both MCN-H_2O_2

244 and MCN-TE-H_2O_2. This is also confirmed by the photocurrent spectra (I_{ph} vs wavelength curves)

245 recorded at constant potential (0.9 V vs Ag/AgCl) and reported in Fig. 1(B). Extrapolating to zero the

246 $(Q_{ph} h\nu)^n$ vs hν plots (see Fig. 1(C)), it was possible to estimate the optical band gap of the materials.

247 Assuming indirect optical transitions (n = 0.5 in Eq. 3), an optical band gap of ~ 2.95 ± 0.05 eV was

248 estimated for MCN and MCN-TE, while a higher value (~ 3 ± 0.05 eV) was estimated for MCN-

249 H_2O_2 and MCN-TE-H_2O_2. The slight discrepancy between the band gap values estimated with DRS

250 and photoelectrochemical measurements can be explained assuming that the allowed energy states

251 close to the valence and conduction band edges are strongly localized due to the formation of a

252 defective material and/or due to the lack of long range order. The contribution to the collected

253 photocurrent from the optical transitions between these localized states is low due to poor generation

254 and transport properties of the photocarriers generated in these states [33].

255 FIGURE 1

256 The photocurrent (I_{ph}) vs electrode potential curves recorded under constant photon energy for all the

257 investigated photocatalysts are reported in Fig. 1(D). There is a clear inversion of the photocurrent

258 sign on going from anodic to cathodic polarization. The inversion photocurrent potential can be

259   assumed as a rough estimation of the flat band potential that is necessary to locate the Fermi level of

260   the materials [34]. The C_3N_4 Fermi level falls within the valence band and conduction band edges of

261   C_3N_4 reported in the literature [6] being slightly more anodic for the MCN-H_2O_2 sample.

262   The photocatalytic activity of the C_3N_4 is assigned to their ability to generate reactive oxygen species

263   (ROS) upon exposure to irradiation. Suitable positions of the CB edge of C_3N_4 towards the one-

264   electron reduction of O_2 determine the generation of $O_2^{\bullet-}$ upon exposure of aerated suspensions.

265   However, in aqueous systems the photogenerated $O_2^{\bullet-}$/$^{\bullet}O_2H$ are readily transformed into H_2O_2, which

266   can be involved in the consecutive reactions giving rise to $^{\bullet}OH$ [12].

FIGURE 2

268   Figure 2(A) illustrates the experimental and simulated EPR spectra of DMPO spin-adducts obtained

269   upon UVA exposure of MCN-TE and MCN-H_2O_2 in aqueous suspension. The dominant twelve-line

270   signal of $^{\bullet}$DMPO-O_2H (spin-Hamiltonian parameters a_N=1.411 mT, a_H^{β}=1.121 mT, a_H^{γ}=0.124 mT;

271   g=2.0058) detected, is superimposed with four-line signal characteristic for the $^{\bullet}$DMPO-OH spin-

272   adduct (a_N=1.494 mT, a_H^{β}=1.466 mT; g=2.0057), and brings evidence on the reduction of O_2 upon

273   exposure of both photocatalysts. However, the observed concentration of spin-adducts was

274   significantly lower for MCN-H_2O_2 representing a defective material. After irradiation stopping, the

275   signal of $^{\bullet}$DMPO-O_2H is transformed to $^{\bullet}$DMPO-OH reflecting the well-known behaviour of

276   $^{\bullet}$DMPO-O_2H in aqueous media. The increased stability of the photogenerated $O_2^{\bullet-}$ in aprotic media

277   is documented in the EPR spectra recorded upon UVA irradiation of MCN-TE and MCN-H_2O_2

278   suspended in DMSO/water mixed solvent (Fig. 2 B,C). The UVA exposure initiates the predominant

279   generation of twelve-line signal of $^{\bullet}$DMPO-O_2^-/O_2H spin-adducts, along with further signals assigned

280   to $^{\bullet}$DMPO-CH_3 and $^{\bullet}$DMPO-OCH_3 produced by the interactions of ROS with DMSO solvent [28]

281   (spin-Hamiltonian parameters Table S2). Figure 2(C) summarizes the concentration of individual

282   DMPO spin-adducts elucidated from the simulation analysis of experimental EPR spectra measured

283   in DMSO/water suspensions of C_3N_4-based photocatalysts. The highest ability to produce $^{\bullet}$DMPO-

284   O_2^-/O_2H spin-adducts was found for MCN-TE, while the ROS formation is suppressed in the case of

285   H_2O_2 treated photocatalysts, which is in good correlation with the photocurrent data.

286   FIGURES 3 and 4

287   As far as the photocatalytic reactivity is concerned, the results are reported in Figures 3 and 4. The

288   partial oxidation of 5-hydroxymethylfurfural (HMF) proceeded giving rise to 2,5-

289   furandicarboxaldehyde (FDC) both under UV and solar irradiation. Figures 3(A) and (B) report the

290   conversion (X) of HMF and the selectivity (S) to FDC, respectively, during the photocatalytic

291   experiments by using UV lamps. Both X and S are reported vs. the cumulative energy entering the

292   photoreactor, which corresponds to 13.3 $kJ \cdot L^{-1}$ in the range 320-400 nm after 4 hours of irradiation.

293   The experiments carried out with HMF under natural solar light are reported in Figures 4(A) and (B),

294   where the results of each experiment, lasting 4 hours, have been reported by considering the

295   cumulative energy entering the photoreactor in the range 320-400 nm. This energy was slightly

296   different from one run to another depending upon the weather conditions, but corresponded roughly,

297   for a fully sunny day to ca. 27 kJ L^{-1}. The highest HMF conversion was observed, both by irradiating

298   with UV or sunlight, in the presence of the MCN-TE sample. It was the most active sample among

299   all the C_3N_4 materials, as before observed [4,26,27]. By using UV or solar irradiation the MCN-TE-

300   H_2O_2 photocatalyst was, together MCN-H_2O_2, the less active sample but the most selective one

301   forming FDC. By comparing the results obtained under UV and solar light irradiation at the same

302   cumulative energy entering in the reactors, it can be observed that the conversion of HMF increased

303   in the presence of MCN-TE and MCN-TE-H_2O_2 samples under solar light, and at the same time the

304   selectivity versus FDC increased only when the runs were carried out in the presence of the two

305   catalysts treated with H_2O_2. Noteworthy, the use of TiO_2 (not shown in Figures 3 and 4) gave rise to

306   the complete oxidation of HMF and the reaction was completely unselective.

307   Photocatalytic experiments carried out by using 4-methoxy benzyl alcohol (4-MBA) indicate that the

308   conversion of 4-MBA by using the C_3N_4 materials was much higher than that obtained for HMF, and

309   the selectivity to 4-MBAD was remarkable in any case. By using the UV lamps (Figures 3 (C) and

                                                                                          12

(D)), the most active materials were MCN-TE and MCN, giving rise to a conversion of ca. 98 and 63

%, respectively and, at the same cumulative energy (13 kJ L^{-1}) under solar irradiation, the conversions

were nearly the same. For all of the samples, the selectivity to aldehyde at the same cumulative energy

was not affected by the light source with the exception of the MCN sample that was more selective

under solar irradiation. For higher values of irradiation time, the 4-MBA conversion increased, and

selectivity to 4-MBAD generally decreased due to the formation of unidentified intermediates,

probably derived from a further oxidation of the aldehyde. The results obtained in the presence of

TiO_2 P25 were modest, probably due to surface deactivation as we have previously observed in gas-

solid regime with aromatic compounds [35]. To explain the high conversion of MBA it is necessary

to remind the electron donating role of the substituent group -O-CH_3 in the aromatic alcohol,

particularly effective in the para position [36].

Photocatalytic experiments carried out by using cinnamyl alcohol (CA) as model molecule under UV

irradiation, shown in Figures 3(E) and (F), indicated that MCN-TE and MCN were also in this case

the most active photocatalysts. By comparing the results obtained under UV and solar light irradiation

at the same cumulative energy entering in the reactors (13 kJ·L^{-1}), CA conversion was higher under

solar irradiation (see Figure 4(E)), for all of the catalysts, but the selectivity (Fig. 4(F)) slightly

decreased. Notably, benzaldehyde was formed in all of the experiments, in agreement with the

literature [37]. Indeed, the partial oxidation of CA gave rise to two aldehydes, mainly cinnamaldehyde

but also benzaldehyde, although in lower amounts.

It can be concluded that the photocatalytic results showed that the materials prepared in the absence

of H_2O_2 were more active both under UV and solar irradiation by using three different model

molecules, particularly MCN-TE, which resulted by EPR investigation the most active generating

$O_2^{\bullet-}$ species and, consequently, the less selective versus the aldehyde formation. The presence of

H_2O_2 during the preparation steps did not give rise to a doped material for MCN-H_2O_2 but to the

formation of a defective powder with lower reactivity than MCN or MCN-TE. Both MCN-TE-H_2O_2

and MCN-H_2O_2 were less effective in forming ROS as they showed the lowest ability to produce

336 •DMPO-O_2^-/O_2H spin-adducts. This fact, that resulted in good agreement with the photocurrent data,

337 can explain why the H_2O_2 treated photocatalysts were less photoactive and more selective towards

338 the aldehyde formation in comparison with the other samples.

339

347

348 **References**

349 [1] X. Lang, X. Chen, J. Zhao, Chem Soc Rev 46 (2014) 473-486.

350 [2] L. Palmisano, V. Augugliaro, M. Bellardita, A. Di Paola, E. García-López, V. Loddo, G. Marcì,

351 G. Palmisano, S. Yurkadal, ChemSusChem 4, 2011) 1431-1438.

352 [3] X. C. Wang, K. Maeda, A. Thomas, K. Takanabe, G. Xin, K. Domen, M. Antonietti, Nat. Mater.

353 8 (2009) 76-80.

354 [4] I. Krivstov, E.I. García-López, G. Marcì, L. Palmisano, Z. Amghouz, J.R. García, S. Ordóñez,

355 E. Díaz, Appl. Catal. B 204 (2017) 430-439.

356 [5] S. Verma, R.B. Nasir Baig, M.N. Nadagouda, R.S. Varma, ACS Sust. Chem. Eng. 4 (2016) 1094-

357 1098.

358 [6] Y.J. Cui, Z.X. Ding, P. Liu, M. Antonietti, X.Z. Fu, X.C. Wang, Phys. Chem. Chem. Phys. 14

359 (2012) 1455-1462.

360 [7] S. Zhang, J. Li, X. Wang, Y. Huang, M. Zeng, J.J. Xu, J. Mater. Chem. A 3 (2015) 10119-10126.

361 [8] H. Yan, Chem. Commun. 48 (2012) 3430-3432.

[9] D. Hollmann, M. Karnahl, S. Tschierlei, K. Kailasam, M. Schneider, J. Radnik, K. Grabow, U. Bentrup, H. Junge, M. Beller, S. Lochbrunner, A. Thomas, A. Brückner, Chem. Mater. 26 (2014) 1727-1733.

[10] E. Morra, E. Giamello, M. Chiesa, J. Magn. Reson. 280 (2017) 89-102.

[11] E.G. Panarelli, S. Livraghi, S. Maurelli, V. Polliotto, M. Chiesa, E. Giamello, J. Photochem. Photobiol. A, 322–323 (2016) 27–34.

[12] J. Xiao, J. Rabeah, J. Yang, Y. Xie, H. Cao, A. Brückner, ACS Catal.7 (2017) 6198-6206.

[13] J.S. Zhang, X.F. Chen, K. Takanabe, K. Maeda, K. Domen, J.D. Epping, X.Z. Fu, M. Antonietti, X.C. Wang, Angew. Chem. Int. Ed. 49 (2010) 441-444.

[14] L. Jiang, X. Yuan, Y. Pan, J. Liang, G. Zeng, Z. Wu, H. Wang, App. Catal. B, 217 (2017) 388-406.

[15] Y. Wang, Y. Di, M. Antonietti, H. Li, X. Chen, X. Wang, Chem. Mater. 22 (2010) 5119-5121.

[16] Y. Wang, H. Li, J. Yao, X. Wang, M. Antonietti, Chem. Sci. 2 (2011) 446-450.

[17] S. Guo, Y. Tang, Y. Xie, C. Tian, Q. Feng, W. Zhou,B. Jiang, Applied Catal B 218 (2017) 664-671.

[18] M. Bellardita E.I. García-López, G. Marcì, I. Krivtsov, J.R. García, L. Palmisano, App. Catal. B 220 (2018) 222-233.

[19] X. Chen, J. Zhang, X. Fu, M. Antonietti, X. Wang, JACS 131 (2009) 11658-11659.

[20] Z.F. Huang, J.J. Song, L. Pan, Z. Wang, X. Zhang, J.J. Zhou, W. Mi, X. Zhang, L. Wang, Nano Energy 12 (2015) 646-656.

[21] J.H. Li, B. Shen, Z.H. Hong, B.Z. Lin, B.F. Gao, Y.L. Chen, Chem. Commun. 48 (2012) 12017-12019.

[22] J.W. Zhang, S. Gong, N Mahmood, L Pan, X. Zhang, J.J. Zou, Appl. Catal B 221 (2018) 9-16

[23] G. Dong, Z. Ai, L. Zhang, RSC Advances 4 (2014) 5553-5560.

[24] K. Li, Z. Huang, X. Zeng, B. Huang, S. Gao, J. Lu, ACS Appl. Mater. Interfaces 9 (2017) 11577-11586

388 [25] M. Ilkaeva, I. Krivtsov, E.V. Bartashevich, S. Khainakov, J.R. García, E. Díaz, S. Ordóñez,

389 Green Chem. 19 (2017) 4299-4304.

390 [26] M. Ilkaeva, I. Krivtsov, E.I. García-López, G. Marcì, O. Khainakova, J.R. García, L. Palmisano,

391 E. Díaz, S. Ordóñez, J. Catal. 359 (2018) 212-222.

392 [27] M. Ilkaeva, I. Krivtsov, J.R. García, E. Díaz, S. Ordóñez, E.I. García-López, G. Marcì, L.

393 Palmisano, M.I. Maldonado, S. Malato, Catal. Today 2018, in press.

394 [28] D.R. Duling, J. Magn. Reson. B, 104 (1994) 105-110.

395 [29] E. Pližingrová, M. Klementová, P. Bezdička, J. Boháček, Z. Barbieriková, D. Dvoranová, M.

396 Mazúr, J. Krýsa, J. Šubrt, V. Brezová, Catal. Today, 281 (2017) 165-180.

397 [30] V. Augugliaro, E.I. García-López, V. Loddo, S. Malato-Rodriguez, I. Maldonado, G. Marcì, R.

398 Molinari, L. Palmisano, Solar Energy. 79 (2005) 402-408.

399 [31] Y. Cui, G. Zhang, Z. Lin, X. Wang, Applied Catal B 181 (2016) 413-419.

400 [32] A. Zaffora, F. Di Franco, M. Santamaria, H. Habazaki, F. Di Quarto, Electrochim. Acta 201

401 (2016) 333-339

402 [33] A. Zaffora, F. Di Franco, M. Santamaria, H. Habazaki, F. Di Quarto, Phys. Chem. Chem. Phys.

403 18 (2016) 351-360

404 [34] A. Zaffora, F. Di Franco, M. Santamaria, H. Habazaki, F. Di Quarto, Electrochim. Acta 180

405 (2015) 666-678.

406 [35] G. Marcì, M. Addamo, V. Augugliaro, S. Coluccia, E. García-López, V. Loddo, G. Martra, L.

407 Palmisano and M. Schiavello, J. Photochem. Photobiol., A: Chem 160 (2003) 105-114.

408 [36] S. Yurdakal, V. Augugliaro, RSC Adv. 2 (2012) 8375-8380.

409 [37] G. Wu, G.L. Brett, E. Cao, A. Costantinou, P. Ellis, S. Kuhn, G.J. Hutchings, D. Bethell, A.

410 Gavridis, Catal. Sci. Technol. 6 (2016) 4749-4758.

411

CAPTION FOR FIGURES

413 Figure 1. (A) dark, D, light, L, current transients; (B) Photocurrent spectra for C_3N_4 samples; (C)

414 Optical band gap estimates and (D) Photocurrent vs. electrode potential curves recorded at 330 nm

415 as irradiating wavelength.

416

417 Figure 2. Experimental (solid line) and simulated (dotted line) EPR spectra (magnetic field sweep

418 width, 7 mT) obtained after UVA photoexcitation (λ_{max} = 365 nm) of MCN-TE and MCN-H_2O_2 in

419 the aerated (A) water or (B) DMSO/water (80:20 v:v) suspensions in the presence of DMPO spin

420 trap. (C) The concentration of DMPO spin-adducts elucidated from the simulation analysis of

421 experimental EPR spectra measured in DMSO/water suspensions of C_3N_4-based samples (amount of

422 C_3N_4 = 0.8 g L^{-1}; C_0(DMPO) = 0.04 M, UVA dose 6 J cm^{-2}).

423

424 Figure 3. Conversion of the alcohol (A), (C) and (E) and selectivity to the aldehyde (B), (D) and (F),

425 during the partial oxidation reaction in the presence of MCN (♦); MCN-TE (■); MCN-TE-H_2O_2 (●);

426 MCN-H_2O_2 (▲) and TiO_2 Evonik P25 (●) for experiments carried out under UV irradiation.

427

428 Figure 4. Conversion of the alcohol (A), (C) and (E) and selectivity to the aldehyde (B), (D) and (F),

429 during the partial oxidation reaction in the presence of MCN (♦); MCN-TE (■); MCN-TE-H_2O_2 (●);

430 MCN-H_2O_2 (▲) and TiO_2 Evonik P25 (●) for experiments carried out under natural solar light
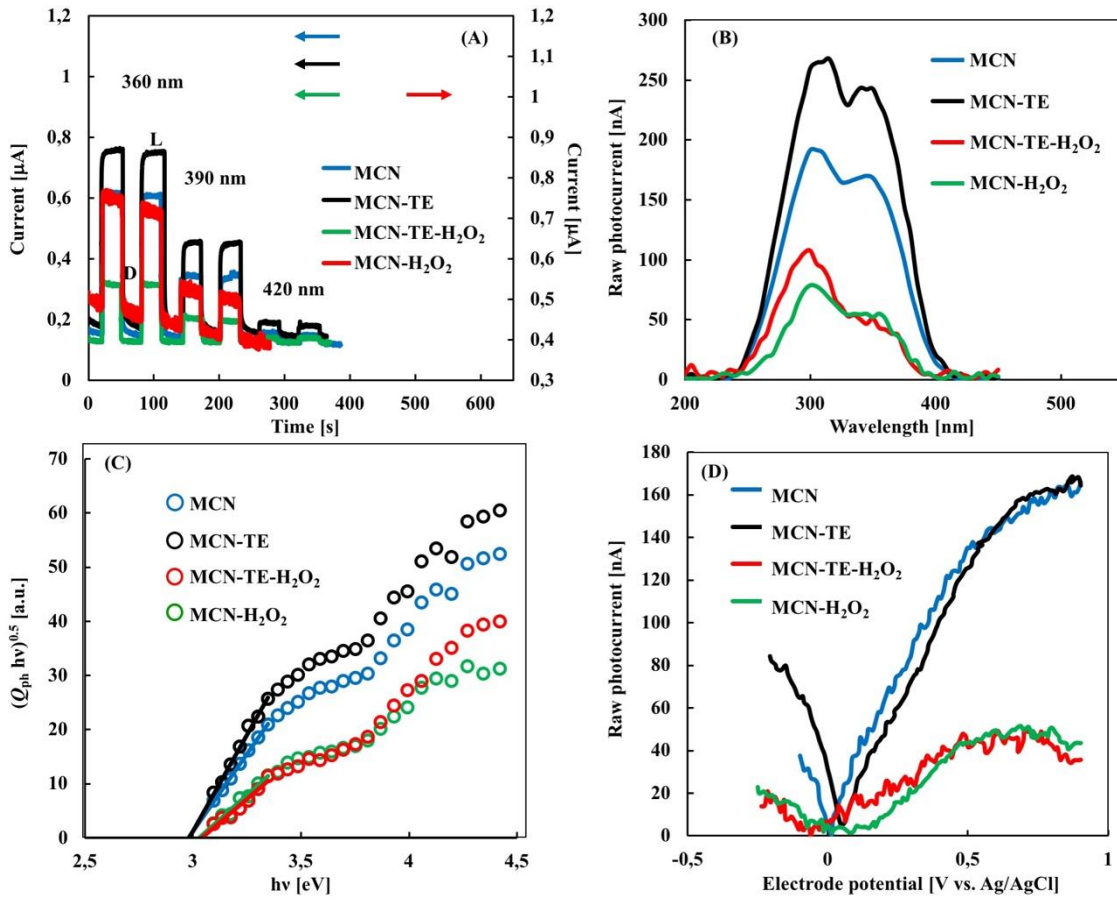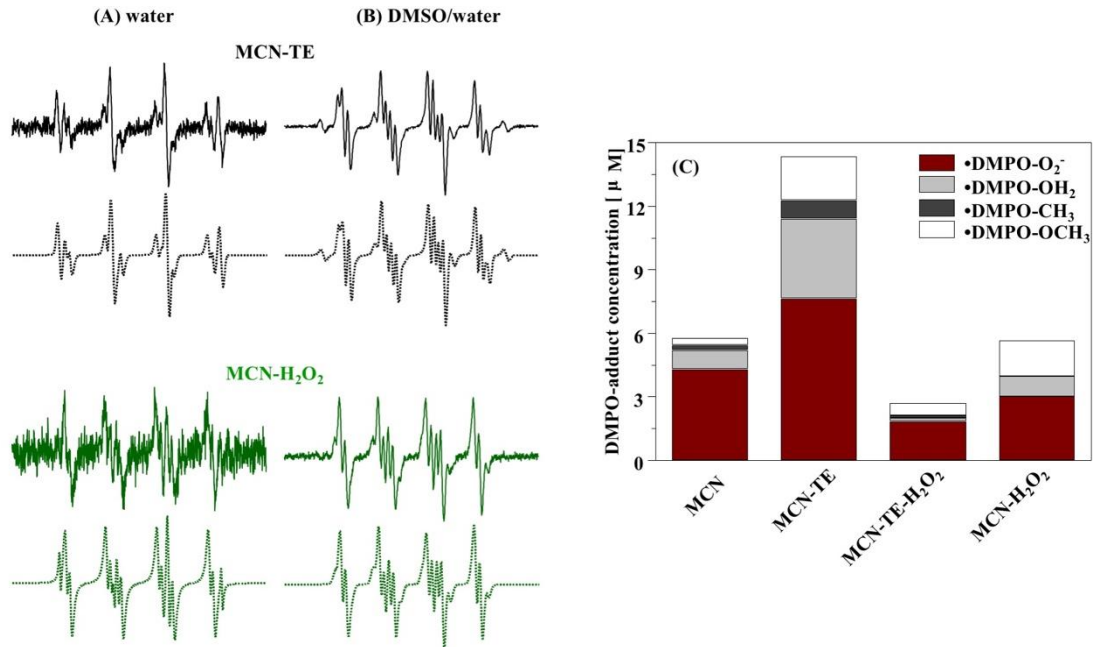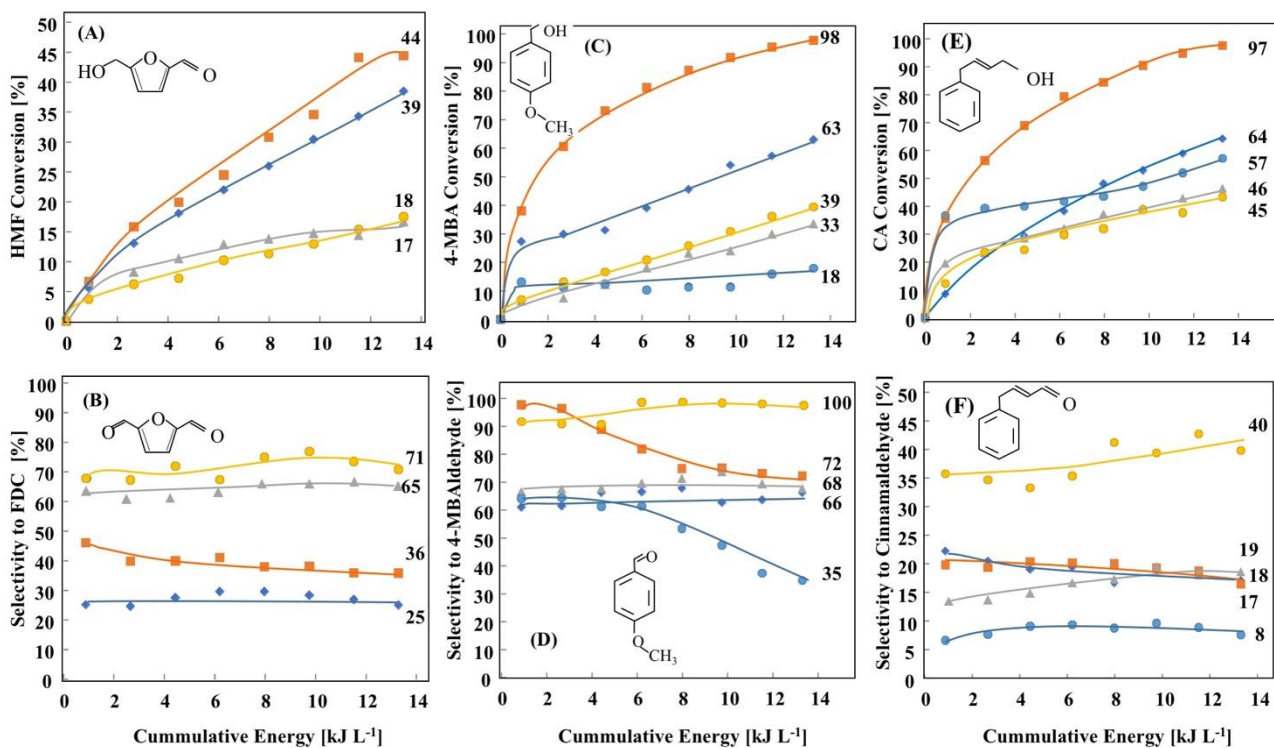
431 irradiation.

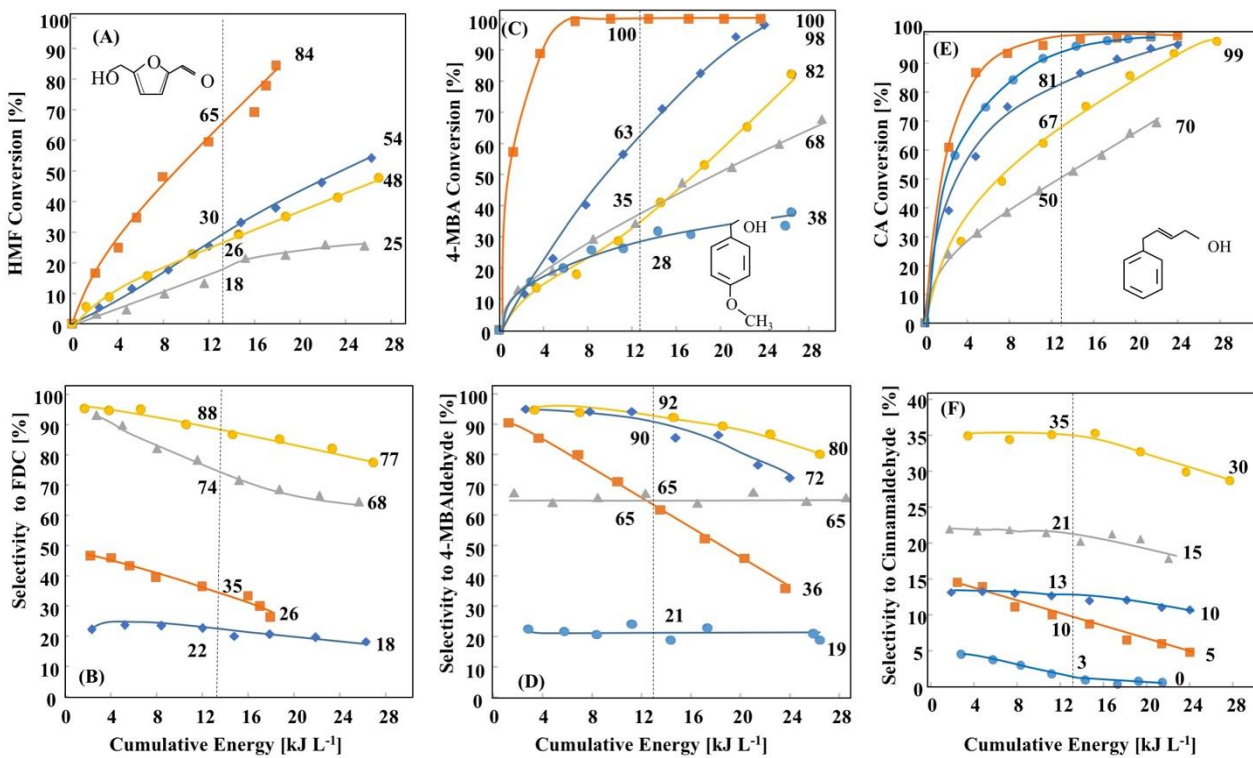432

433   FIGURE 1

FIGURE 2

434

FIGURE 3

435

FIGURE 4

436